

# Mechanistic insights into Z-ring formation and stability: A Langevin dynamics approach to FtsZ self-assembly

Rajneesh Kumar,<sup>1,\*</sup> Ramanujam Srinivasan,<sup>2,3,†</sup> and Debasish Chaudhuri<sup>1,3,‡</sup>

<sup>1</sup>*Institute of Physics, Sachivalaya Marg, Sainik School, Bhubaneswar 751005, India*

<sup>2</sup>*National Institute of Science Education and Research, Khurda 752050, Odisha, India*

<sup>3</sup>*Homi Bhabha National Institutes (HBNI), Training School Complex, Anushakti Nagar, Mumbai, India 400094*

The tubulin-like protein FtsZ is crucial for cytokinesis in bacteria and many archaea, forming a ring-shaped structure called the Z-ring at the site of cell division. Despite extensive research, the formation of Z-rings is not entirely understood. We propose a theoretical model based on FtsZ's known filament structures, treating them as semiflexible polymers with specific mechanical properties and lateral inter-segment attraction that can stabilize ring formations. Our Langevin dynamics simulations reveal various morphological phases, including open helices, chains, rings, and globules, capturing experimental observations in the fission yeast model using FtsZ from different bacterial species or mutants of *Escherichia coli*. Using the theoretical model, we explore how treadmilling activity affects Z-ring stability and identify a spooling mechanism of ring formation. The active ring produces contractile, shear, and rotational stresses, which intensify before the Z-ring transitions to an open helix at high activity.

## I. INTRODUCTION

FtsZ is one among the diverse family of bacterial cytoskeletal proteins that exhibits distinct homologies to eukaryotic tubulin [1–4]. In prokaryotic cells, e.g., bacteria and many archaea, FtsZ (filamenting temperature-sensitive mutant Z) proteins assemble into a ring, the Z-ring, at the future division site, and it attaches to the cell membrane [5, 6]. This ring provides the backbone for the formation of divisome [7, 8], a complex multi-protein structure that recruits other proteins required for septum formation between dividing cells. Moreover, the Z-ring itself may generate a constriction force helping cytokinesis [9].

Assembly of FtsZ into a ring-like structure requires polymerization of the monomeric units of FtsZ, which, like tubulin, depends on the binding of the nucleotide GTP [10–14]. Although GTP hydrolysis triggers the disassembly of FtsZ filaments, the assembly and polymerization of FtsZ itself is required for the GTPase activity. This is because GTP is sandwiched in the interface between two subunits of FtsZ, and while one subunit binds GTP, the catalytic residue necessary to hydrolyze the terminal phosphate in GTP is provided by the adjoining subunit [13, 15, 16]. GTP hydrolysis rates in FtsZ polymers regulate the turnover rates of the filaments [17–19] and, more recently, have been shown to drive treadmilling activity in FtsZ filaments [20–22]. *In vivo*, FtsZ filaments are dynamic. They are seen to organize as spiral structures along the axis of the cell during the cell elongation and condense into a ring (Z-ring) during cytokinesis, which is tightly coupled to the cell cycle progression [23–25]. In *Bacillus subtilis*, such spiral FtsZ

filaments have been seen to coalesce into a ring during sporulation [23]. Other studies have also suggested a spiral or helical intermediate in the formation of the cytokinetic FtsZ ring [26]. However, despite numerous earlier studies, the exact mechanisms of FtsZ ring formation are not fully understood.

FtsZ is not only indispensable for cell division but is also the first protein to localize to the division site and orchestrates the recruitment of more than a dozen other proteins required for septation [1, 27–30]. FtsZ is also thought to be an ancient protein that originated as soon as cells formed during an early stage of genetic code evolution [31]. Thus, understanding FtsZ function and its assembly into the cytokinetic ring remains a fundamental question central to biology. FtsZ, therefore, has received extensive attention in the past decades, both in experiments [17, 32–35] and in numerical studies [36–42]. Numerical studies in two dimensions showed that lateral attraction plays a crucial part in determining the final shape of the FtsZ filament [43]. However, this model [43] lacked spontaneous torsion, which, as shown recently in Ref. [44], is important in generating the required constriction force. In recent years, considerable advancements have been made in comprehending the role, function, and mechanisms of FtsZ, particularly how it produces constriction force on the membrane.

The FtsZ filaments constituting rings are found to be highly dynamic [17, 20, 32, 45]. Recently, it has been shown that treadmilling not only guides the cell wall synthesis machinery [21, 22, 46, 47] but also plays a crucial role in FtsZ ring assembly [49]. FtsZ polymerizes and forms a large variety of dynamic structures, straight, bent, and helical filaments, which are highly dependent on the experimental conditions such as pH, the presence of various monovalent salts, crowding agents, and polycations [50]. Using the structure of crystallized *Methanococcus jannaschii* FtsZ dimer and numerical simulations, the torsional and bending curvatures of FtsZ filaments were extracted [51]. The intrinsic torsional

\* rajneesh.kumar@iopb.res.in

† rsrini@niser.ac.in

‡ debc@iopb.res.in

curvature present in the FtsZ could deform the membranes via torsional stress and show chiral treadmilling vortices *in vivo* [52]. Earlier experiments also suggested that GTPase activity and concentration of free  $\text{Mg}^{2+}$  ions play an important role in the dynamics and ring formation [53, 54], and free  $\text{Mg}^{2+}$  ions favor the lateral contacts between the filaments.

While these *in vivo* and *in vitro* reconstitution experiments have generated deep insights into the assembly dynamic of FtsZ filaments, a slightly different approach to studying bacterial cytoskeleton assembly in a molecularly crowded cellular environment was taken by Balasubramanian and colleagues [19]. The authors expressed FtsZ in yeast cells, both budding yeast (*Saccharomyces cerevisiae*) as well as fission yeast (*Schizosaccharomyces pombe*), and showed that FtsZ can assemble into a ring-like structure even in the absence of all other bacterial cytokinetic proteins [19]. They further showed that the process of ring assembly involves a spooling-like mechanism, possibly driven by GTP hydrolysis and lateral associations among the FtsZ filaments.

In this paper, we aim to understand the mechanisms behind the emergence of observed FtsZ filament morphologies in both bacterial and yeast systems using a polymer model and Langevin dynamics simulations. Our theoretical approach assumes the existence of FtsZ filamentous assembly as the starting point. We model it as a tangentially active chiral semiflexible polymer characterized by finite bending and torsional rigidity, as well as intrinsic bending and torsional curvatures. A tangential activity is used to model the FtsZ treadmilling. Our primary achievements are: (i) Our model accurately captures all experimentally observed FtsZ morphologies, such as rings, helices, filaments, and globules, observed in FtsZ from different bacterial species or FtsZ mutants of *Escherichia coli*. (ii) A minimal lateral attraction is necessary for ring formation, and treadmilling can flatten and widen globules into rings, displaying rotation and a spooling mechanism to ring formation. (iii) The ring state remains stable over a broad range of treadmilling activities before transitioning into the open helix (OH) through phase coexistence. We obtain a detailed phase diagram, with the phase boundaries marked by peaks in size fluctuations and extensile response. (iv) Active spinning chiral rings (SCR) induce contractile stresses, rotation, and shear that intensify near the phase boundaries.

The paper is organized as follows: In Sec. II, we first summarise the experimental results, setting the motivation for the theoretical study. In Sec. III, we present the model and simulation details. In Sec. IV, we discuss the main results, including the phase diagram, shape and size of the polymer, and stress generation. Finally, we conclude in Sec. V, summarizing our results and presenting an outlook.

## II. EXPERIMENTAL RESULTS: MOTIVATION FOR THEORY

The various shapes of FtsZ assemblies, like rings, helices, filaments, and condensates that have been found in several *in vitro* experiments and *in vivo* studies in bacteria have also been observed for several kinds of FtsZs expressed in fission yeast. Fission yeast has served as a useful model to study the assembly dynamics of ring formation by FtsZ [19]. FtsZ from different bacterial species or FtsZ mutants of *Escherichia coli* have been shown to assemble into different forms such as helices [55] (*Helicobacter pylori* FtsZ or HpFtsZ), rings [19, 55] (EcFtsZ, *Staphylococcus aureus* SaFtsZ and EcFtsZ Q47K), globules (EcFtsZ D209A), open chains (EcFtsZ Q47K and EcFtsZ Q47KD86K), closed chains (EcFtsZ Q47KD86K) and network of polymers [19] (EcFtsZ and EcFtsZ G105S). The different forms of FtsZ assemblies that have been thus far seen upon expression in fission yeast are shown in Fig.1(a). Further, since linear and helical polymers of FtsZ have been shown to undergo a transition into rings, or vice-versa in yeast and bacterial systems [19, 23, 24], the forms observed for the FtsZ mutants in yeast cells might suggest that the mutations drive and stabilize one or the other states. Dynamics of EcFtsZ Q47K ring formation in fission yeast (*S. pombe*) from an open chain shows a spooling mechanism.

As revealed by independent electron microscopy studies [56], the filaments observed in fluorescent microscopy Fig. 1(a) are typically filament bundles composed of multiple FtsZ chains bound laterally to each other. In the following section, we present a polymer model for such filament bundles.

## III. MODEL

We consider an active bead-spring chain with bending and torsional rigidity to model the FtsZ filament. The polymer is denoted by a space curve described by position vectors  $\{\mathbf{r}_1, \mathbf{r}_2 \dots, \mathbf{r}_N\}$  corresponding to  $N$  beads. The bonding energy is given by  $U_b = \frac{k_S}{2} \sum_{i=1}^{N-1} (|\mathbf{b}_i| - r_0)^2$  where the bond vector  $\mathbf{b}_i = \mathbf{r}_{i+1} - \mathbf{r}_i$ , the rest-length of the bonds is  $r_0$ , and  $k_S$  is the bond stiffness. The bending energy is given by  $U_\theta = \frac{\kappa_\theta}{2} \sum_{i=1}^{N-2} (\theta_i - \langle \theta \rangle)^2$ , where  $\theta_i$  is the angle between two consecutive bond vectors  $\mathbf{b}_i$  and  $\mathbf{b}_{i+1}$ , and  $\kappa_\theta$  denotes the bending modulus. The non-planar nature of the space curve is described by the dihedral angle  $\delta_i$  between two successive planes constituted of bond-vectors  $\{\mathbf{b}_i, \mathbf{b}_{i+1}\}$  and  $\{\mathbf{b}_{i+1}, \mathbf{b}_{i+2}\}$  involving three successive segments. The torsional energy of the chain is modeled by  $U_\phi = \frac{\kappa_\phi}{2} \sum_{i=1}^{N-3} (\phi_i - \langle \phi \rangle)^2$ , where  $\kappa_\phi$  is the torsional modulus.

The self-avoidance and lateral attraction in the chain are modeled using an interaction potential  $U_{NB}$  between

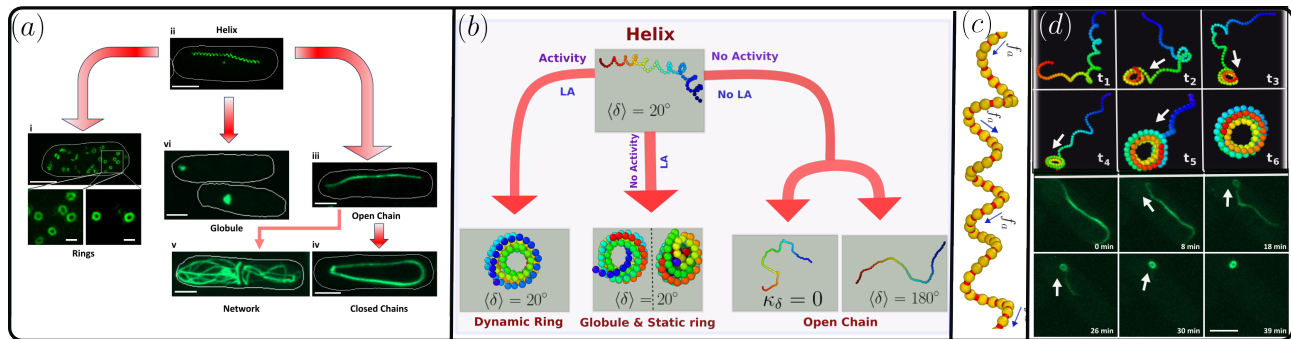


Figure 1. (a) Images showing the various forms of FtsZ polymers when expressed in fission yeast. (i) ring-like structures of *E. coli* FtsZ (EcFtsZ), (ii) helical or spiral polymers of *Helicobacter pylori* FtsZ, (iii) straight linear polymers (open chains) of EcFtsZ Q47KD86K mutant, (iv) closed loops (closed chains) formed by EcFtsZ Q47KD86K mutant, (v) flexible polymers or networks formed by FtsZ G105S mutant and (vi) blobs or globules formed by the GTPase catalytic mutant EcFtsZ D209A. The scale bar represents  $3\mu\text{m}$ . (b) Schematic diagram of the active chains studied at different parameter regimes and lateral attraction (LA), recapitulating conformations in (a). (c) Schematic representation of the active chain with active force  $f_a$  acting tangentially along the chain's backbone. (d) Spooling dynamics of ring formation: Configurations of the active chain in the presence of lateral attraction at  $Pe = 1$  and  $\tilde{\epsilon} = 1$  at different stages of ring formation with time  $t_i$ . Dynamics of EcFtsZ Q47K ring formation in fission yeast (*S. pombe*) from an open chain. Time-lapse imaging shows the different stages of ring assembly (time is in minutes). In this study, all plots of the model polymer are generated using Ovito [57], and the filament color coding from blue to red represents the filament's tail to head, the direction of treadmilling.

non-bonded monomers, with

$$U_{\text{NB}}(r) = \begin{cases} \sum_{\langle i,j \rangle} 4\epsilon \left[ \left( \frac{\sigma}{r_{ij}} \right)^{12} - \left( \frac{\sigma}{r_{ij}} \right)^6 \right] + \epsilon & \text{for } r_{ij} \leq r_{\text{min}} \\ 0 & \text{for } r_{ij} > r_{\text{min}}. \end{cases} \quad (1)$$

A choice of  $r_{\text{min}} = 2^{1/6}\sigma$  makes the above potential purely repulsive, the Weeks-Chandler-Andersen (WCA) interaction. This choice can model a self-avoidance. In addition, attraction between filament segments can be incorporated by replacing the distance cutoff by the typical Lennard-Jones (LJ) choice  $r_{\text{min}} = 2.5\sigma$  so that monomers at a separation beyond the WCA cutoff attract each other via the LJ potential. The total energy cost is  $U = U_b + U_\theta + U_\phi + U_{\text{NB}}$ .

We model the treadmilling activity in terms of a tangential active force  $f_a \mathbf{b}_i$  that acts along each bond. Here  $f_a$  denotes a force per unit length [58]. This leads to a total self-propulsion force  $\mathbf{F}_a = \sum_{i=1}^{N-1} f_a \mathbf{b}_i$ . We use the dimensionless Péclet number,

$$Pe = \frac{f_a r_0^2}{k_B T}, \quad (2)$$

to characterize the local activity. Note that, for a chain of length  $L = (N-1)r_0$ , a related measure of activity  $Pe_L = Pe(L/r_0)^2$  that scales quadratically with the chain length has been used in recent studies of active polymers [58].

The Langevin dynamics of the chain are described by

$$m\dot{\mathbf{v}}_i = -\nabla_i U - \gamma \mathbf{v}_i + \gamma\sqrt{2D} \boldsymbol{\eta}_i + \mathbf{f}_a^i. \quad (3)$$

where,  $\mathbf{f}_a^i = f_a \mathbf{u}_i$  with  $\mathbf{u}_i = (\mathbf{b}_{i-1} + \mathbf{b}_i)/2$  for  $i = 2, \dots, (N-1)$  and  $\mathbf{u}_1 = \mathbf{b}_1/2$ ,  $\mathbf{u}_N = \mathbf{b}_{N-1}/2$ . In the absence of active drive, the above equation obeys equilibrium fluctuation-dissipation with monomer diffusivity

$D = k_B T / \gamma$ , and Gaussian random noise  $\boldsymbol{\eta}_i$  satisfying  $\langle \boldsymbol{\eta}_i \rangle = 0$  and  $\langle \boldsymbol{\eta}_i(t) \otimes \boldsymbol{\eta}_j(t') \rangle = \delta_{ij} \delta(t-t') \mathbf{1}$ . The length, energy, and time scales are set by  $\sigma = r_0$ ,  $k_B T$ , and  $\tau = \sigma \sqrt{m/k_B T}$ , where  $\tau$  also describes the time scale for diffusion over  $\sigma$ . In these units, we choose  $k_S = 100$  and set  $\kappa_\theta / \kappa_\phi = 2.915$ ,  $\langle \theta \rangle = 7.6^\circ$  and  $\langle \phi \rangle = 20^\circ$  in accordance with previous all-atom simulations that were in agreement with properties of wild-type FtsZ filaments [51]. Further, we choose  $\kappa_\theta = 20$ , such that the ratio of the chain length  $L$  to the persistence length  $\ell_p$  of the polymer,  $L/\ell_p = 5$ , consistent with measured persistence lengths [19] (also see Appendix-A). The strength of the inter-segment attraction is tuned using the dimensionless control parameter  $\tilde{\epsilon} = \epsilon/k_B T$ . The Langevin dynamics simulations are performed using  $\delta t = 10^{-4} \tau$  within the velocity-Verlet implementation in LAMMPS [59] with in-house modifications to incorporate the tangential activity.

## IV. RESULTS

FtsZ filaments exhibit a variety of structural forms, including helices, rings, open filaments, and globules, as shown in Fig.1(a) and captured within our model, Fig.1(b). In the absence of lateral attraction (WCA repulsion between segments) and activity, the model proposed above leads to a native state of equilibrium helical configurations [51]. This conformation can be seen in the top panel of Fig.1(b). Such morphologies can relax to simple equilibrium open chains in the absence of helicity in two limits of (i) vanishing torsional rigidity or (ii) intrinsic curvature  $\langle \phi \rangle = \pi$  constraining polymeric fluctuations to an arbitrary plane. Examples of such



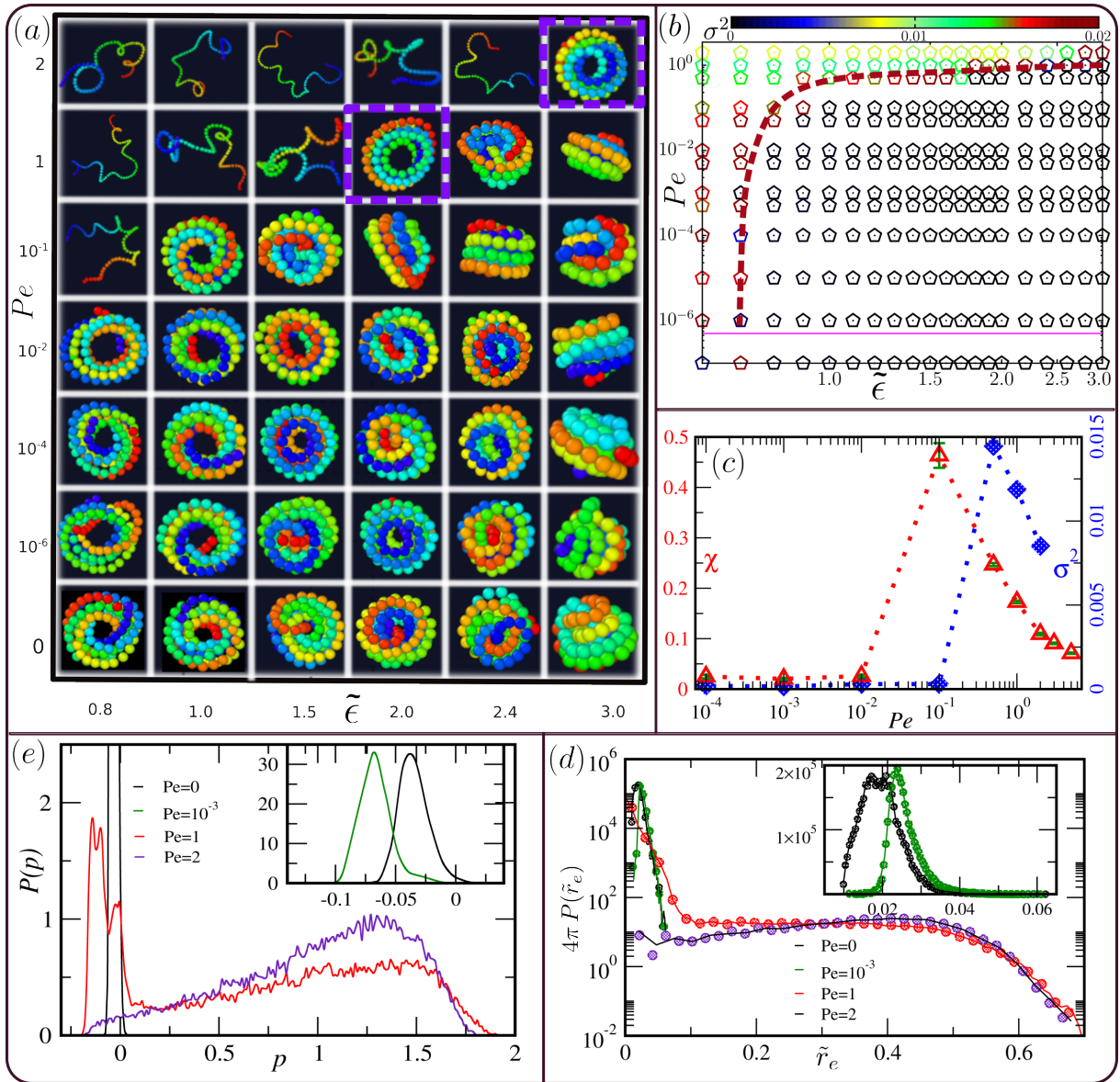


Figure 3. (a) Configurational phase diagram in the  $Pe - \tilde{\epsilon}$  plane. The active chains are color-coded from the tail (blue) to the head (red), with self-propulsion directed from the tail to the head. Note that in terms of an alternative measure  $Pe(L/r_0)^2$ , the polymer activity in the figure ranges from 0 to  $2 \times 10^4$ . (b) Quantitative phase diagram in the  $Pe - \tilde{\epsilon}$  plane using fluctuations  $\sigma^2 = \langle \tilde{r}_e^2 \rangle - \langle \tilde{r}_e \rangle^2$  of the scaled end-to-end separation  $\tilde{r}_e = r_e/L$  represented by points denoted by colors as shown in the color bar. (c) Plot of  $\sigma^2$  as a function of  $Pe$  for a fixed  $\tilde{\epsilon} = 1$  and shows a maximum at  $Pe^* = 0.5$  and decreases away from this point. The plot is shown by blue ( $\diamond$ ) data points and the axis label on the right. The extension modulus  $\chi$  is plotted with the red-colored left axis and red ( $\triangle$ ) data points.  $\chi$  exhibits a non-monotonic increase with activity  $Pe$  and peaks near the transition point  $Pe^{**} = 0.1$ . The green-colored symbol denotes a representative error bar. (d) Probability distributions  $p(\tilde{r}_e)$  for various  $Pe$  values at  $\tilde{\epsilon} = 2$ . The clear bimodality in the distribution function at  $Pe = 1$  shows the coexistence of compact globule and ring structures with open helical conformation. Inset: compares the distributions at  $Pe = 0$  and  $10^{-3}$ . (e) Probability distributions  $P(p)$  of the prolateness  $p$  for the same  $Pe$  values as in (d) and  $\tilde{\epsilon} = 2$ . At  $Pe = 1$ , the distribution shows maxima corresponding to globule (peak around  $p = 0$ ), ring (peaks at  $p \approx -0.1$  and  $-0.15$ ), and open helix (peak for  $p \approx 1.5$ ).

while the height of this pillbox-shape  $\lambda_3$  remains smaller. With increasing  $\tilde{\epsilon}$ ,  $\lambda_1 = \lambda_2$  shrinks, and the  $\lambda_3$  increases to become equal at the formation of spherical globule at  $\tilde{\epsilon} = 3$ . Note that the transformation of the ring state to the globule is gradual and does not show any signature

of phase transition. As we show in the later section, the presence of treadmilling activity can transform a globule into a ring, thereby potentially stabilizing rings in the biological context.

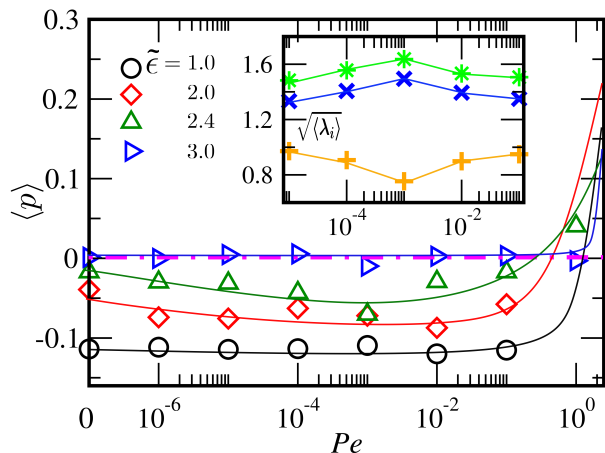


Figure 4. The mean prolateness  $\langle p \rangle$  as a function of activity  $Pe$  for various  $\tilde{\epsilon}$  values. The globule formed at equilibrium condition ( $Pe = 0$ ) transitions into a ring shape as a function of activity ( $Pe$ ). Solid lines are guides to the eye. Inset: Variation of principal radii of gyration,  $\lambda_i$ 's, with  $Pe$  at  $\tilde{\epsilon} = 2.4$ , with symbols for  $i = 1$  (\*),  $i = 2$  (x) and  $i = 3$  (+).

### B. Role of treadmilling activity

The shape of the equilibrium ring formed at  $\tilde{\epsilon} \approx 1$  remains intact over a wide range of treadmilling activity  $Pe$ . Before opening up, the ring shows chiral rotation, characterizing the non-equilibrium SCR state. However, for higher  $\tilde{\epsilon}$  that stabilize globular structures at equilibrium, activity helps to unwind the globule to form rotating rings, thereby stabilizing SCR. At even higher  $Pe$ , the rings do unfold into open helices. For example, at  $\tilde{\epsilon} \approx 1$ , the ring opens up into a helix above  $Pe \approx 0.1$ .

We present a comprehensive phase diagram in Fig. 3(a) and (b) as a function of treadmilling activity  $Pe$  and lateral attraction strength  $\tilde{\epsilon}$ . Fig. 3(a) illustrates representative conformations of the chain at different parameter values. This plot shows representative conformations at  $\tilde{\epsilon} \geq 0.8$  where the equilibrium chain is already in a ring or globule state. For a similar but more detailed phase diagram, see Appendix- B. At any given  $\tilde{\epsilon}$ , the ring destabilizes at high enough  $Pe$  to form an open helix. At small to intermediate  $\tilde{\epsilon}$ , the figure suggests that the ring state remains stable over a broad range of  $Pe$ . However, at high enough  $\tilde{\epsilon}$  (e.g., at  $\tilde{\epsilon} \approx 2.4$ ), the equilibrium chain is in a globule state. With increasing  $Pe$ , the globule first transitions to SCR before undergoing a transition to open helix at high enough  $Pe$  ( $\approx 1$ ) as shown in Fig. 4

In Fig. 3 (b), we present a quantitative version of the phase diagram using fluctuations in the chain's end-to-end separation. The color bar indicates the amount of fluctuations  $\sigma^2 = \langle \tilde{r}_e^2 \rangle - \langle \tilde{r}_e \rangle^2$  in the scaled end-to-end separation  $\tilde{r}_e = r_e/L$ , where  $L$  is the chain length. Near the transition from ring to open helix denoted by the dashed red line in Fig. 3(b),  $\sigma^2$  reaches a maximum. Fig. 3(c) shows the variation of  $\sigma^2$  as a function of  $Pe$  for a fixed  $\tilde{\epsilon} = 1$  (blue colored points and ordinate label)

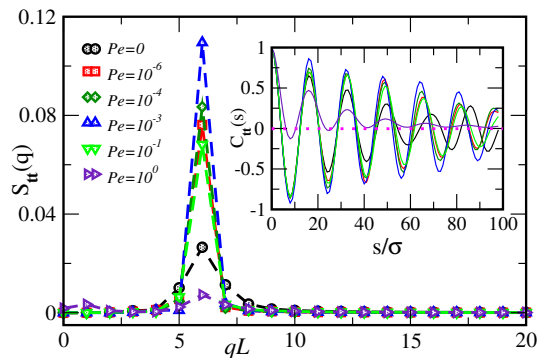


Figure 5. Fourier transform  $S_{tt}(q)$  of the tangent-tangent correlation function  $C_{tt}(s)$  for the helical chain for various  $Pe$  values at fixed lateral attraction  $\tilde{\epsilon} = 1.0$ . The correlation function is oscillatory for the ring phase, with the periodicity captured by the peak in the structure factor. The peak height quantifies the degree of helicity of the chain, while the width of the peak indicates the statistical dispersion of the structure.

with the maximum at  $Pe^* = 0.5$ , the transition point. It sharply diminishes away from this transition point.

This figure also shows the linear response  $\chi$  of the polymer extension under external force (see Appendix-C and Fig.9). It varies non-monotonically with  $Pe$  and shows a maximum that precedes the maximum in  $\sigma^2$ , e.g., at  $Pe^{**} = 0.1$  for  $\tilde{\epsilon} = 1$ . The maximum is attributable to the instability of the ring structure near the transition, where even a small amount of extensile force is sufficient to destabilize the ring and open it.

In Fig. 3(d) and (e), we present the probability distributions  $p(\tilde{r}_e)$  and prolateness  $p$  respectively, at various  $Pe$  keeping  $\tilde{\epsilon} = 2$  fixed. The distribution functions are normalized to  $\int_0^1 d\tilde{r}_e 4\pi\tilde{r}_e^2 P(\tilde{r}_e) = 1$ . At  $Pe = 0$  and  $10^{-3}$ , where the ring phase is stable, the distribution shows a single peak near  $\tilde{r}_e \approx 0.03$ ; see Fig. 3(d) and its inset. The compact structure at equilibrium swells under activity  $Pe = 10^{-3}$  to become more ring-like. Near the transition point,  $Pe = 1$ , the chain shows bimodality in  $P(\tilde{r}_e)$ , indicating the coexistence of open helix (maximum near  $\tilde{r}_e = 0.45$ ) and compact ring (maximum near  $\tilde{r}_e \lesssim 0.01$ ). At higher  $Pe$ , the distribution becomes unimodal with a maximum around  $\tilde{r}_e = 0.45$  for  $Pe = 2$ , corresponding to the open helix. The broad distribution characterizes large deviations around this maximum, allowing the chain to visit other conformations.

The distribution of prolateness  $p$  remains unimodal at  $Pe = 0$  and  $10^{-3}$  (Fig. 3(e) and inset). The location of the maximum shifts towards smaller  $p$  values at  $Pe = 10^{-3}$ , with respect to equilibrium. This is due to the reorganization to a better ring via the non-equilibrium swelling. At  $Pe = 1$ , the multimodal distribution function  $P(p)$  displays the coexistence of ring, globule, and open helix, captured by the peaks at  $p < 0$ ,  $p \approx 0$ , and  $p > 0$ , respectively. Moreover, at this Péclet, the distribution shows a second maximum with split peaks at  $p < 0$ . The first one near  $p = -0.1$  corresponds

to the stable ring phase. The second one at  $p < -0.1$  corresponds to a more swollen ring that is formed on the way of opening up from the ring state to the open helical conformation. The reduction of  $p$  with swelling can be understood using larger  $\lambda$  in Eq.(7). At a higher activity,  $Pe = 2$ , as the chain opens up, the distribution becomes unimodal again with one maximum near  $p \approx 1.25$ .

The variation of mean prolateness  $\langle p \rangle$  with  $Pe$  corresponding to different  $\tilde{\epsilon}$  is shown in Fig.4. The equilibrium ring state at  $\tilde{\epsilon} = 1$  remains relatively unaltered up to  $Pe \approx 0.1$ , where the ring transitions into an open helix. On the other hand,  $\langle p \rangle$  increases with  $\tilde{\epsilon}$  at  $Pe = 0$  to vanish at large  $\tilde{\epsilon}$ , as the equilibrium ring gets into globule-like shape; see Fig.2 as well. With increasing  $Pe$ , the equilibrium globules at  $\tilde{\epsilon} = 2$  and 2.4 become ring-like, showing a decrease in  $\langle p \rangle$  reaching a negative minimum at an intermediate value of  $Pe$  ( $Pe = 10^{-3}$ ) before increasing with activity as the rings open up. This suggests that treadmilling activity can regulate the formation of FtsZ rings. This feature is further characterized using the three principal radii of gyration  $\langle \lambda_i \rangle^{1/2}$  with  $i = 1, 2, 3$ , for  $\tilde{\epsilon} = 2.4$  shown in the inset of Fig.4. At  $Pe = 10^{-3}$ ,  $\langle \lambda_1 \rangle$  and  $\langle \lambda_2 \rangle$  becomes largest as the ring widens and associated with this  $\langle \lambda_3 \rangle$  gets to the smallest value signifying the maximal thinning of the ring.

The change in mean size and shape of the active chiral chain can further be analyzed in terms of the mean radius of gyration, asphericity, and prolateness. For example, see Appendix-D and Fig.10.

The number of turns in the SCR does not change before it opens up; however, the robustness of the ring state varies non-monotonically. This is established using the tangent-tangent correlation function  $C_{\mathbf{t}\mathbf{t}}(s) = \langle \mathbf{t}(s) \cdot \mathbf{t}(0) \rangle$  along the chain contour, and its Fourier transforms  $S_{\mathbf{t}\mathbf{t}}(q)$ ; see Fig.5. The correlation function shows periodic variation with the periodicity captured by the pronounced maximum in  $S_{\mathbf{t}\mathbf{t}}(q)$  with the location of the maximum near  $q = n/L$  denoting the number of turns  $n$ . Fig.5 shows the maximum is at  $n = qL \approx 6$ . As we see, this position of maximum does not change with  $Pe$ ; however, the height of  $S_{\mathbf{t}\mathbf{t}}(q)$  at the maximum varies non-monotonically. The initial increase with  $Pe$  characterizes the formation of a more stable ring. The subsequent decrease of this peak height at even larger  $Pe$  signifies the destabilization of the ring.

### 1. Dynamics near the SCR-open helix phase boundary

The dynamics of the chain near the spiral to open helix transition can be analyzed using the time series of the principal radii of gyration  $\lambda_i$  with  $i = 1, 2, 3$  and the prolateness  $p$ ; see Fig. 6. The time series in Fig. 6(a) shows signatures of a coexisting compact ring (denoted by  $R1$ ), swelled ring ( $R2$ ), globule ( $G$ ), and open helix ( $OH$ ). The globule is characterized by  $\lambda_1 = \lambda_2 = \lambda_3$  and  $p = 0$ . The data at  $G$  shows approximate agreement with this expectation. In the ring state,  $\lambda_1 \approx \lambda_2$  is signif-

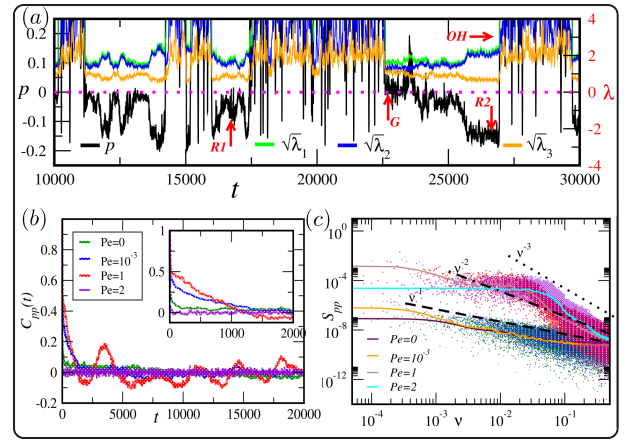


Figure 6. (a) A representative time series of  $p$  and the principal radii of gyration at  $Pe = 1$  and  $\tilde{\epsilon} = 2$  where ring (marked with  $R1$ ,  $R2$ ), globule ( $G$ ) and open helix ( $OH$ ) co-exist. Here  $R1$  and  $R2$  represent the compact and swollen ring states with  $p = -0.1$  and  $p = -0.15$ , respectively. (b) Two-time auto-correlation function of  $p$  for various  $Pe$  values at  $\tilde{\epsilon} = 2$ . (c) Power spectral densities  $S_{pp}(\nu)$  for the same  $\tilde{\epsilon}$  and  $Pe$  values as in (b). The scatter plots denote the direct Fourier transform, and the solid lines are guides to the eye. The black dashed, dash-dotted and dotted lines represent  $\nu^{-1}$ ,  $\nu^{-2}$  and  $\nu^{-3}$ , respectively.

icantly larger than  $\lambda_3$  and  $p(R2) < p(R1)$  with both  $R1$  and  $R2$  rings having negative  $p$ . For  $OH$ ,  $\lambda_1 \gg \lambda_2 (\approx \lambda_3)$  and  $p \rightarrow 2$  (also see Fig.11 in Appendix-E).

These dynamics can be further characterized in terms of two-time correlations and the corresponding power spectral density. Fig. 6(b) shows the correlation function  $C_{pp}(t) = \langle \delta p(t) \delta p(0) \rangle / \langle \delta p^2(0) \rangle$  with  $\delta p(t) = p(t) - \langle p \rangle$ . The corresponding power spectrum  $S_{pp}(\nu)$  is obtained by Fourier transforming the correlation function and is plotted in Fig. 6(c). We used TISEAN [64] to compute the correlation and power spectrum. The apparent oscillations in  $C_{pp}(t)$  at  $Pe = 1$  correspond to the phase coexistence. The absence of any characteristic maximum in frequency  $\nu$  in the power spectrum  $S_{pp}(\nu)$  characterizes the absence of any robust oscillation in the dynamics. The high frequency behavior of  $S_{pp}$  shows approximate power-law decay as  $\nu^{-\beta}$  with  $\beta = 1$  in the stable SCR phase ( $Pe = 0$  and  $10^{-3}$ ),  $\beta = 2$  for  $Pe = 1$  near the transition, and  $\beta = 3$  for  $Pe = 2$  corresponding to open helix.

### 2. Stress generation by the spinning chiral ring

Here, we present a direct measure of the active stress due to the spinning chiral ring (SCR). Recent advances led to derivations of swim pressure for active Brownian particles [65–68]. Instead, we employ an embedding environment to calculate the stress due to the active chain.

We consider a harmonic cubic lattice of size  $N_g^3$  with fixed boundaries to embed the SCR. The lattice spacing

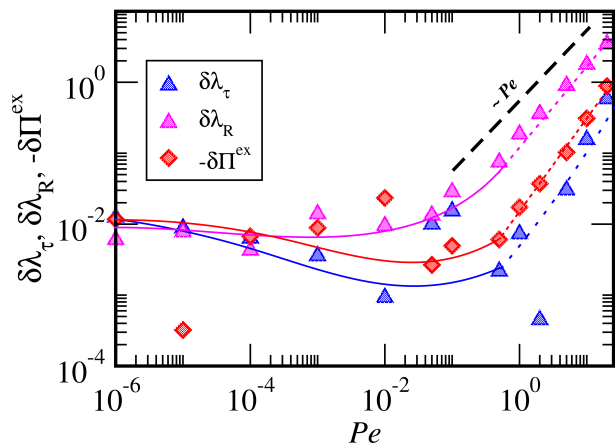


Figure 7. Deviations of excess pressure  $\delta\Pi^{ex}$ , magnitude of the largest eigenvalue of shear  $\delta\lambda_\tau$ , and the largest eigenvalue of rotation  $\delta\lambda_R$  from their equilibrium values  $\Pi^{ex}|_{eq} = 0.8734$ ,  $\lambda_\tau|_{eq} = 0.1757$  and  $\lambda_R|_{eq} = 0.0034$ . The black dashed line represents linear growth  $\sim Pe$ . Solid and dashed lines serve as visual guides, with dashed lines indicating the  $Pe$  range in which the free chain opens up into a helix.

is chosen to be  $\sigma$  and  $N_g = 17$  such that the box size  $N_g\sigma$  is significantly larger than the diameter of the SCR so that the distortions do not reach the boundaries. The monomers of the chain are assumed to be bonded with lattice points within the cutoff distance  $\sigma$ . To avoid introducing new parameters, we choose these bond strengths and that of the harmonic lattice to be  $k_S$ , the same as in the active polymer.

We calculate the excess stress on the cubic lattice due to the active chiral chain

$$\Sigma_{\alpha\beta} = -\frac{1}{\mathcal{N}\sigma^3} \sum_{i=1}^{\mathcal{N}} \langle r_{i\alpha} f_{i\beta} \rangle, \quad (8)$$

where  $\mathcal{N}$  denotes the number of lattice points bonded with the chain, and  $\mathcal{N}\sigma^3$  is the corresponding volume occupied by them. Here,  $f_{i\beta}$  stands for the  $\beta$ -th component of the force acting on the lattice point  $i$  due to the chain.

The stress tensor  $\Sigma_{\alpha\beta}$  is fully characterized by its three irreducible parts, the excess pressure  $\Pi^{ex}$ , shear  $\tau_{\alpha\beta}$ , and rotation  $R_{\alpha\beta}$ . They are expressed as

$$\begin{aligned} \Pi^{ex} &= -\frac{1}{d} \Sigma_{\alpha\alpha} \\ \tau_{\alpha\beta} &= \frac{1}{2} (\Sigma_{\alpha\beta} + \Sigma_{\beta\alpha}) - \frac{1}{d} \Sigma_{\alpha\alpha} \delta_{\alpha\beta} \\ R_{\alpha\beta} &= \frac{1}{2} (\Sigma_{\alpha\beta} - \Sigma_{\beta\alpha}), \end{aligned} \quad (9)$$

where  $d$  is the embedding dimension. The Einstein summation convention is assumed above. The pressure is a scalar,  $\tau_{\alpha\beta}$  is a traceless symmetric matrix, and  $R_{\alpha\beta}$  is a purely antisymmetric matrix. In our study  $d = 3$ . Thus, in 3d, shear  $\tau_{\alpha\beta}$  has five independent components, and rotation  $R_{\alpha\beta}$  has three.

In Fig. 7, we show the dependence of the  $\Pi^{ex}$ , the magnitude of the largest eigenvalues  $\lambda_\tau$  of  $\tau_{\alpha\beta}$  and the largest eigenvalue  $\lambda_R$  of  $R_{\alpha\beta}$  as a function of activity. We show the deviations of these quantities from equilibrium values (at  $Pe = 0$ ) with increasing  $Pe$ . The deviation in excess pressure  $\delta\Pi^{ex}$  is negative, showing that the activity of the chain generates contractility, as expected from experimental observations. The deviations in shear  $\delta\lambda_\tau$  and rotation  $\delta\lambda_R$  show similar dependence on activity; see Fig. 7. For activity higher than  $Pe = 1$ , at which the SCR is unstable towards the open helix, all the above measures show a linear increase with  $Pe$ .

## V. CONCLUSIONS

Our study addresses the pivotal question of how treadmilling and lateral attraction contribute to the formation of the FtsZ filament's ring structure during cell division. Using a coarse-grained theoretical model that treats FtsZ filaments as tangentially active chiral semiflexible polymers, we accurately reproduced various morphological phases observed experimentally, including rings, helices, filaments, and globules. While lateral attraction stabilizes the ring structure, it fails to induce the observed net rotation without treadmilling activity. We presented a detailed phase diagram exploring ring stability as a function of activity and attraction, revealing a stable ring state over a broad range of treadmilling activity before transitioning into an open helix through phase coexistence, indicative of a first-order phase transition. In fact, treadmilling flattens and widens otherwise globule states to stabilize SCR and generates contractile stresses in their surroundings. The transition from the stable ring state to the open helix state is marked by increased size fluctuations and extensile response. While our model treats FtsZ as an assembled polymer, we recognize that the Z-ring's structure is more intricate. It forms from multiple shorter treadmilling filaments near a curved membrane surface, merging to create the Z-ring. Models that capture this initial assembly, incorporating treadmilling rates, and account for filament ordering on a curved membrane could offer further insights into bacterial cytokinetic ring formation. Our findings, nonetheless, enhance the understanding of FtsZ ring dynamics and provide a basis for further study into bacterial cytokinesis regulation and the evolutionary link between FtsZ protofilaments and microtubule structures.

## VI. ACKNOWLEDGEMENT

The numerical simulations were performed using SAMKHYA, the High-Performance Computing Facility provided by the Institute of Physics, Bhubaneswar. Image credits: Authors acknowledge Ajay Kumar Sharma and Sakshi Mahesh Poddar for FtsZ images and Mirza Salim Beg at the Center for Interdisciplinary Sciences at

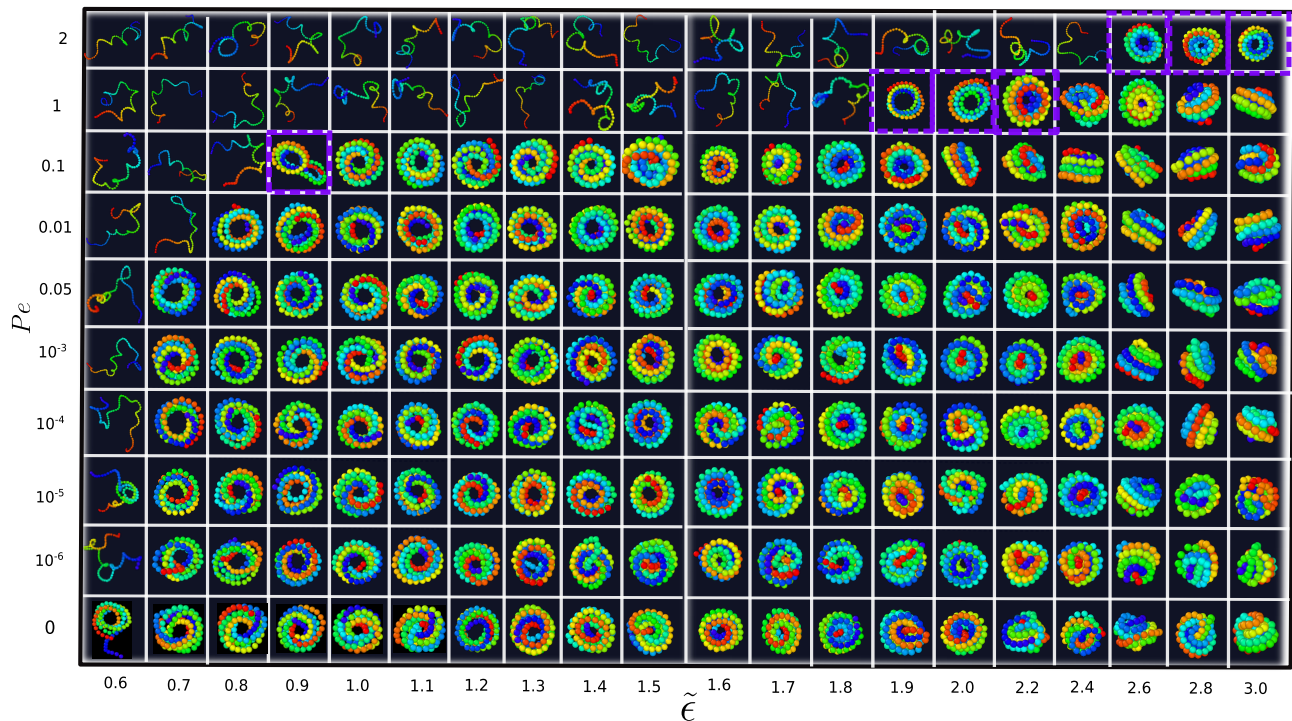


Figure 8. Configurational phase diagram in the  $Pe - \tilde{\epsilon}$  plane. The system exhibits various structures across different ranges of activity  $Pe$  and lateral attraction strength  $\tilde{\epsilon}$ . The chain maintains a stable helical structure for very low values of  $\tilde{\epsilon}$  and forms a ring at intermediate  $\tilde{\epsilon}$  values across a broad range of  $Pe$ . At higher  $\tilde{\epsilon}$  and lower  $Pe$  values, the chain adopts globule structures. Increased  $Pe$  tends to favor an open chain conformation by disrupting contacts between chain segments. Violet square boxes denote the coexistence of ring, globule, and open helical structures forming near transition points, where the chain spends maximum time in an open conformation and also forms structures like rings or globules. Note that in terms of another measure of activity defined earlier in Sec. III,  $Pe$  ranges from  $10^{-2}$  to  $2 \times 10^4$ .

NISER, Jatni. We thank Amir Shee and Subhashree S Khuntia for the FtsZ persistence length analysis. DC acknowledges a research grant from the Department of Atomic Energy (DAE), India (1603/2/2020/IoP/R&D-II/150288) and thanks the International Centre for Theoretical Sciences (ICTS-TIFR), Bangalore, for an Associateship. RS acknowledges funding support from NISER, DAE.

data sets	$L$	$\ell_p$	$\frac{\Delta \ell_p}{\ell_p}$	$L/\ell_p$
1	250	63.39	3.93%	3.94
2	290	60.84	2.57%	4.76
3	376	65.26	2.42%	5.76

Table I. The values of  $L$  and  $\ell_p$  listed in the table are in units of pixels where each pixel has a size  $0.0346 \mu\text{m}$ . The length of the chains are  $L \sim 10 \mu\text{m}$ , and vary between  $8 \mu\text{m}$  to  $13 \mu\text{m}$ . The effective persistence length  $\ell_p \approx 2 \mu\text{m}$ , equivalent to wild type FtsZ values measured earlier [19].

### Appendix A: Persistence length of open chains

We used movies of the FtsZ mutant EcFtsZ Q47KD86K that remains in open chain conformation to extract effective persistence length  $\ell_p$  by evaluating tangent-tangent correlation and fitting with  $\langle \hat{u}(s) \cdot \hat{u}(0) \rangle = \exp(-s/\ell_p)$  over shorter length scales. We used FIJI to extract the chain conformation on which we performed the analysis. The correlation over longer separations is known to deviate from exponential to power-law decay due to, e.g., self-avoidance.

### Appendix B: Configurational phase diagram

The main text presents a configurational phase diagram for a few selected parameter values in the  $Pe - \tilde{\epsilon}$  plane. In Fig. 8, we show a full conformational phase diagram over a wider range of parameter values.

### Appendix C: Extensile response

In Fig. 9, we show the change in the end-to-end distance along the  $x$ -direction with respect to the steady state distance  $\delta x_e$  ( $:= \langle x_e \rangle_{f_s} - \langle x_e \rangle_{f_s=0}$ ) as a function of the applied stretching force  $f_s$  at different  $Pe$  and fixed

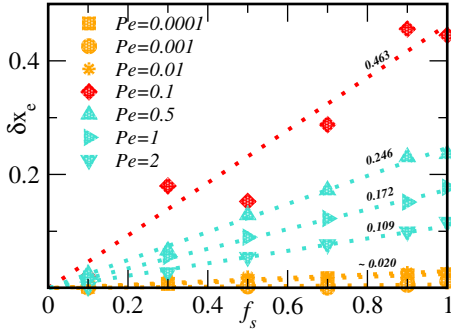


Figure 9. Extension  $\delta x_e$  as a function of external force  $f_s$  for various values of  $Pe$  and fixed  $\tilde{\epsilon} = 1$ . The data points are color-coded: orange for the ring phase, turquoise for the open helix conformations, and red indicating the transition point ( $Pe = 0.1$ ). Dotted lines depict linear fits to the data for various  $Pe$  with their respective slope values.

$\tilde{\epsilon} = 1$ . For all  $Pe$  values,  $\delta x_e$  scale linearly with small  $f_s$  as shown with the dotted lines in Fig. 9. The linear fits are used to calculate the extensile linear response  $\chi = \frac{\partial \delta x_e}{\partial f_s}$  used in the main text. Note that because of self-avoidance, compression of the rings that already have a compact structure is strongly resisted, and the slope of the response sharply changes for negative  $f_s$ .

#### Appendix D: Size and shape of the polymer chain

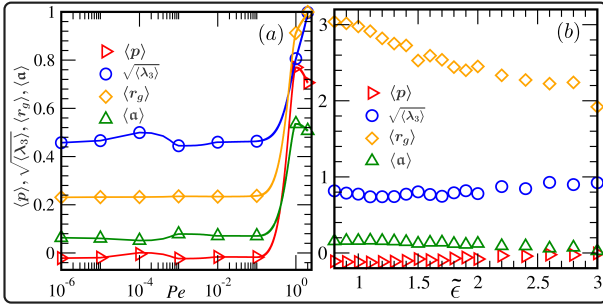


Figure 10. Radius of gyration ( $r_g$ ), asphericity ( $\mathbf{a}$ ), thickness ( $\sqrt{\lambda_3}$ ); smallest eigenvalue of the radius of gyration tensor) and prolateness ( $p$ ) as function of  $Pe$  for fixed lateral attraction  $\tilde{\epsilon} = 1$  (a) and as a function of  $\tilde{\epsilon}$  for fixed  $Pe = 10^{-2}$  (b). In panel (a), radius of gyration is scaled by  $r_g^{(max)} = 14.39$  and thickness by  $\sqrt{\lambda_3}^{(max)} = 2.4$  that are the value of  $r_g$  and  $\sqrt{\lambda_3}$ , respectively, for  $Pe = 2$ .

As shown in the main text, the size and shape of a polymer can be quantified using the eigenvalues of the radius of gyration tensor, specifically using the radius of gyration  $r_g$  (Eq. 5) and prolateness  $p$  (Eq. 6). In addition, here we use the asphericity  $\mathbf{a}$  of a configuration, given by

$$\mathbf{a} = \frac{3 \sum_{i=1}^3 (\lambda_i - \frac{\lambda_{tr}}{3})^2}{\lambda_{tr}^2} = 1 - 3 \frac{\lambda_d}{\lambda_{tr}^2} \quad (\text{D1})$$

where  $\lambda_d = \lambda_1 \lambda_2 + \lambda_2 \lambda_3 + \lambda_3 \lambda_1$ . The mean asphericity  $\langle \mathbf{a} \rangle$  is obtained by averaging over steady-state configurations. For a perfect isotropy  $\langle \mathbf{a} \rangle = 0$  and  $\langle p \rangle = 0$ . The asphericity  $\mathbf{a}$  is bounded above and below  $0 \leq \mathbf{a} \leq 1$ .

In Fig. 10(a), we show the variation of all these parameters as activity increases at  $\tilde{\epsilon} = 1$ . For a wide range of activities ( $10^{-6} \leq Pe \leq 10^{-1}$ ) rings are stable with  $\langle r_g \rangle$ ,  $\langle p \rangle < 0$ ,  $\langle \mathbf{a} \rangle > 0$  remaining unchanged. Note that  $\langle \lambda_3 \rangle$  is a measure of ring thickness in the SCR phase. This also remains unchanged up to  $Pe = 0.1$ . At high enough activity,  $Pe > 0.1$ , intersegment attraction gets overpowered by activity to break contacts between the monomers and destabilize the ring to open a helix state. Examples of the equilibrium ring and active rotating SCR are shown in Supplemental Movie 2. In Fig. 10(b), we show the variation of the same size and shape parameters as a function of  $\tilde{\epsilon}$  at a fixed  $Pe = 10^{-2}$ . Increasing  $\tilde{\epsilon}$  shrinks the size  $\langle r_g \rangle$ . A clear crossover from ring to globule is captured by the vanishing of  $\langle p \rangle$  and  $\langle \mathbf{a} \rangle$ .

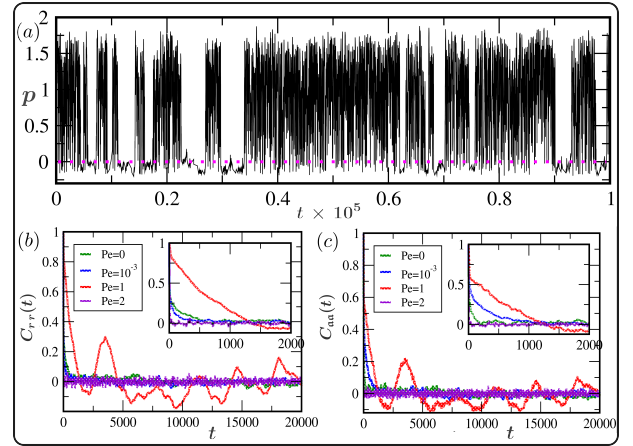


Figure 11. (a) Full time series of prolateness  $p$  at  $Pe = 1$  and  $\tilde{\epsilon} = 2$  where ring (marked with  $R1$ ,  $R2$ ), globule ( $G$ ) and open helix ( $OH$ ) co-exist. The dashed magenta line corresponds to  $S = 0$ . (b), (c) are two-time auto-correlation functions of radius of gyration ( $r_g$ ) and asphericity ( $\mathbf{a}$ ), respectively, for various  $Pe$  values at  $\tilde{\epsilon} = 2$ .

#### Appendix E: Dynamics: Time-series and correlation

Here, we show a long-time series of prolateness  $-1/4 \leq p \leq 2$  near a transition point  $\tilde{\epsilon} = 2$  and  $Pe = 1$ . The value of  $p$  shows large excursions between open helix (large positive  $p$ ), globule  $p = 0$ , and ring  $p < 0$  states; see Fig. 11(a). The correlation functions  $C_{rr}(t) = \langle \delta r_g(t) \delta r_g(0) \rangle / \langle \delta r_g^2(0) \rangle$  for the radius of gyration  $r_g(t)$  and  $C_{aa}(t) = \langle \delta \mathbf{a}(t) \delta \mathbf{a}(0) \rangle / \langle \delta \mathbf{a}^2(0) \rangle$  asphericity  $\mathbf{a}(t)$  show similar features as that of  $C_{pp}(t)$  shown in the main text. The apparent oscillations in the correlations at  $Pe = 1$  do not correspond to any specific oscillatory Fourier mode, as verified using the corresponding power spectra having features similar to  $S_{pp}(\nu)$  shown in the main text.

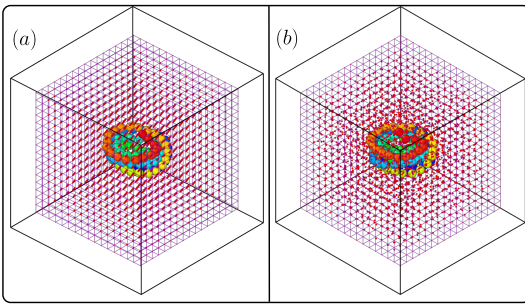


Figure 12. (a) The cubic lattice embedding the active ring. The boundary points (small red-colored spheres) at the six faces remain fixed, while the rest of the lattice can distort. The monomers of the chain are bonded with the lattice points within a cutoff distance  $\sigma$ . (b) A typical configuration with distortion of the lattice at  $Pe = 1$ . The bounding box, indicated by black lines, is solely for visual representation.

## Appendix F: Distortion of embedding matrix

Fig. 12(a) shows the initial cubic lattice with the active ring embedded in it. Fig. 12(b) shows a typical steady-state configuration with the distortion of the lattice points and stretching of the bonds at  $Pe = 1$ .

- 
- [1] E. Bi and J. Lutkenhaus, Ftsz ring structure associated with division in escherichia coli, *Nature* **354**, 161 (1991).
- [2] D. W. Adams and J. Errington, Bacterial cell division: assembly, maintenance and disassembly of the z ring, *Nat. Rev. Microbiol* **7**, 642 (2009).
- [3] H. P. Erickson, D. E. Anderson, and M. Osawa, Ftsz in bacterial cytokinesis: Cytoskeleton and force generator all in one, *Microbiology and Molecular Biology Reviews* **74**, 504 (2010).
- [4] J. F. Lutkenhaus, H. Wolf-Watz, and W. D. Donachie, Organization of genes in the ftsa-enva region of the escherichia coli genetic map and identification of a new fts locus (ftsZ), *J Bacteriol.* **142**, 615 (1980).
- [5] D. P. Haeusser and W. Margolin, Splitsville: structural and functional insights into the dynamic bacterial z ring, *Nat. Rev. Microbiol.* **14**, 305 (2016).
- [6] C. Ortiz, P. Natale, L. Cueto, and M. Vicente, The keepers of the ring: regulators of ftsZ assembly, *FEMS microbiology reviews* **40**, 57 (2015).
- [7] M. Vicente, A. I. Rico, and J. Martnez-Arteaga, Roco and Mingorance, Septum enlightenment: assembly of bacterial division proteins, *J Bacteriol.* **188**, 19 (2006).
- [8] N. Nanninga, Cell division and peptidoglycan assembly in escherichia coli, *Mol Microbiol* **5**, 791 (1991).
- [9] M. Osawa, D. E. Anderson, and H. P. Erickson, Reconstitution of Contractile FtsZ Rings in Liposomes, *Science* (80-. ). **320**, 792 (2008).
- [10] P. d. Boer, R. Crossley, and L. Rothfield, The essential bacterial cell-division protein FtsZ is a GTPase, *Nature* **359**, 254 (1992).
- [11] D. RayChaudhuri and J. T. Park, Escherichia coli cell-division gene ftsZ encodes a novel GTP-binding protein, *Nature* **359**, 251 (1992).
- [12] A. Mukherjee and J. Lutkenhaus, Guanine nucleotide-dependent assembly of FtsZ into filaments, *Journal of Bacteriology* **176**, 2754 (1994).
- [13] J. Lwe and L. A. Amos, Crystal structure of the bacterial cell-division protein FtsZ, *Nature* **391**, 203 (1998).
- [14] E. Nogales, K. H. Downing, L. A. Amos, and J. Lwe, Tubulin and FtsZ form a distinct family of GTPases, *Nature Structural Biology* **5**, 451 (1998).
- [15] J. M. Wagstaff, M. Tsim, M. A. Oliva, A. Garca-Sanchez, D. Kureisaite-Ciziene, J. M. Andreu, and J. Lwe, A Polymerization-Associated Structural Switch in FtsZ That Enables Treadmilling of Model Filaments., *mBio* **8**, e00254 (2017).
- [16] S. Du, S. Pichoff, K. Kruse, and J. Lutkenhaus, FtsZ filaments have the opposite kinetic polarity of microtubules, *Proceedings of the National Academy of Sciences* **115**, 10768 (2018).
- [17] D. Anderson, F. J. Gueiros-Filho, and H. P. Erickson, Assembly dynamics of ftsz rings in bacillus subtilis and escherichia coli and effects of ftsz-regulating proteins, *J. Bacteriol.* **186**, 57755781 (2004).
- [18] D. W. Adams, L. J. Wu, L. G. Czaplowski, and J. Errington, Multiple effects of benzamide antibiotics on FtsZ function, *Molecular Microbiology* **80**, 68 (2011).
- [19] R. Srinivasan, M. Mishra, L. Wu, Z. Yin, and M. K. Balasubramanian, *Genes Dev.* **22**, 1741 (2008).
- [20] D. A. Ramirez-Diaz, D. A. Garca-Soriano, A. Raso, J. Mcksch, M. Feingold, G. Rivas, and P. Schwill, Treadmilling analysis reveals new insights into dynamic FtsZ ring architecture., *PLoS Biology* **16**, e2004845 (2018).
- [21] X. Yang, Z. Lyu, A. Miguel, R. McQuillen, K. C. Huang, and J. Xiao, GTPase activity-coupled treadmilling of the bacterial tubulin FtsZ organizes septal cell wall synthesis., *Science* **355**, 744 (2017).
- [22] J. W. McCausland, X. Yang, G. R. Squyres, Z. Lyu, K. E. Bruce, M. M. Lamanna, B. Sderstrm, E. C. Garner, M. E. Winkler, J. Xiao, and J. Liu, Treadmilling FtsZ polymers drive the directional movement of sPG-synthesis enzymes via a Brownian ratchet mechanism, *Nature Communications* **12**, 609 (2021).
- [23] S. Ben-Yehuda and R. Losick, Asymmetric cell division in b. subtilis involves a spiral-like intermediate of the cytokinetic protein ftsz, *Cell* **109**, 257 (2002).
- [24] S. Thanedar and W. Margolin, Ftsz exhibits rapid movement and oscillation waves in helix-like patterns in escherichia coli, *Curr Biol.* **14**, 1167 (2004).

- [25] G. Fu, T. Huang, J. Buss, C. Coltharp, Z. Hensel, and J. Xiao, In Vivo Structure of the *E. coli* FtsZ-ring Revealed by Photoactivated Localization Microscopy (PALM), *PLoS ONE* **5**, e12680 (2010).
- [26] L. G. Monahan, A. Robinson, and E. J. Harry, Lateral FtsZ association and the assembly of the cytokinetic Z ring in bacteria, *Molecular Microbiology* **74**, 1004 (2009).
- [27] C. A. Hale and P. A. d. Boer, Direct Binding of FtsZ to ZipA, an Essential Component of the Septal Ring Structure That Mediates Cell Division in *E. coli*, *Cell* **88**, 175 (1997).
- [28] S. Pichoff and J. Lutkenhaus, Unique and overlapping roles for ZipA and FtsA in septal ring assembly in *Escherichia coli*, *The EMBO Journal* **21**, 685 (2002).
- [29] S. Pichoff and J. Lutkenhaus, Tethering the Z ring to the membrane through a conserved membrane targeting sequence in FtsA, *Molecular Microbiology* **55**, 1722 (2005).
- [30] D. S. Weiss, J. C. Chen, J. M. Ghigo, D. Boyd, and J. Beckwith, Localization of FtsI (PBP3) to the septal ring requires its membrane anchor, the Z ring, FtsA, FtsQ, and FtsL., *Journal of Bacteriology* **181**, 508 (1999).
- [31] B. K. Davis, Molecular evolution before the origin of species, *Progress in Biophysics and Molecular Biology* **79**, 77 (2002).
- [32] J. Stricker, P. Maddox, E. Salmon, and H. P. Erickson, Rapid assembly dynamics of the *Escherichia coli* ftsz-ring demonstrated by fluorescence recovery after photobleaching, *Proc. Natl. Acad. Sci. U. S. A.* **99**, 31713175 (2002).
- [33] L. Romberg and P. A. Levin, Assembly dynamics of the bacterial cell division protein ftsz: poised at the edge of stability, *Annu. Rev. Microbiol.* **57**, 125154 (2003).
- [34] C. R. Mahone and E. D. Goley, Bacterial cell division at a glance, *J Cell Sci.* **133**, 7 (2020).
- [35] B. E. Walker, J. Mnnik, and J. Mnnik, Transient membrane-linked ftsz assemblies precede z-ring formation in *Escherichia coli*, *Curr. Biol.* **30**, 499508 (2020).
- [36] B. Ghosh and A. Sain, Origin of contractile force during cell division of bacteria, *Phys. Rev. Lett.* **101**, 178101 (2008).
- [37] C. Lu, M. Reedy, and H. P. Erickson, Straight and curved conformations of ftsz are regulated by gtp hydrolysis, *J. Bacteriol.* **182**, 164170 (2000).
- [38] J. F. Allard and E. N. Cytrynbaum, Force generation by a dynamic z-ring in *Escherichia coli* cell division, *Proc. Natl. Acad. Sci. U. S. A.* **106**, 145150 (2008).
- [39] H. P. Erickson, Modeling the physics of ftsz assembly and force generation, *Proc. Natl. Acad. Sci. U. S. A.* **106**, 92389243 (2009).
- [40] L. T. Nguyen, C. M. Oikonomou, and G. J. Jensen, Simulations of proposed mechanisms of ftsz-driven cell constriction, *Journal of Bacteriology* **203**, e00576 (2021).
- [41] P. Mateos-Gil, P. Tarazona, and M. Vlez, Bacterial cell division: modeling FtsZ assembly and force generation from single filament experimental data., *FEMS Microbiology Reviews* **43**, 73 (2019).
- [42] L. C. Corbin and H. P. Erickson, A unified model for treadmilling and nucleation of single-stranded FtsZ protofilaments., *Biophysical Journal* **119**, 792 (2020).
- [43] I. Hrger, E. Velasco, J. Mingorance, G. Rivas, P. Tarazona, and M. Vlez, Langevin computer simulations of bacterial protein filaments and the force-generating mechanism during cell division, *Phys. Rev. E* **77**, 011902 (2008).
- [44] D. A. Ramirez-Diaz, A. Merino-Salomn, F. Meyer, M. Heymann, G. Rivas, M. Bramkamp, and P. Schwill, FtsZ induces membrane deformations via torsional stress upon GTP hydrolysis, *Nature Communications* **12**, 3310 (2021).
- [45] Y. Chen, K. Bjornson, S. D. Redick, and H. P. Erickson, A Rapid Fluorescence Assay for FtsZ Assembly Indicates Cooperative Assembly with a Dimer Nucleus, *Biophysical Journal* **88**, 505 (2005).
- [46] A. W. Bisson-Filho, Y.-P. Hsu, G. R. Squyres, E. Kuru, F. Wu, C. Jukes, Y. Sun, C. Dekker, S. Holden, M. S. VanNieuwenhze, Y. V. Brun, and E. C. Garner, Treadmilling by FtsZ filaments drives peptidoglycan synthesis and bacterial cell division., *Science* **355**, 739 (2017).
- [47] K. D. Whitley, J. Grimshaw, D. M. Roberts, E. Karinou, P. J. Stansfeld, and S. Holden, Peptidoglycan synthesis drives a single population of septal cell wall synthases during division in *Bacillus subtilis*, *Nature Microbiology* , 1 (2024).
- [48] S. Schper, A. D. Brito, B. M. Saraiva, G. R. Squyres, M. J. Holmes, E. C. Garner, Z. Hensel, R. Henriques, and M. G. Pinho, Cell constriction requires processive septal peptidoglycan synthase movement independent of FtsZ treadmilling in *Staphylococcus aureus*, *Nature Microbiology* , 1 (2024).
- [49] K. D. Whitley, C. Jukes, N. Tregidgo, E. Cesbron, P. Almada, Y. Cesbron, R. Henriques, C. Dekker, and S. Holden, Ftsz treadmilling is essential for z-ring condensation and septal constriction initiation in *Bacillus subtilis* cell division, *Nat. Commun.* **12**, 2448 (2021).
- [50] D. Popp, M. Iwasa, H. P. Erickson, A. Narita, M. Y., and R. Robinson, Suprastructures and dynamic properties of mycobacterium tuberculosis, *J. Biol. Chem.* **285**, 1128111289 (2010).
- [51] P. Gonzalez de Prado Salas, I. Hrger, F. Martn-Garca, J. Mendieta, . Alonso, M. Encinar, P. Gmez-Puertas, M. Vlez, and P. Tarazona, Torsion and curvature of ftsz filaments, *Soft Matter* **10**, 1977 (2014).
- [52] D. A. Ramirez-Diaz, D. A. Garca-Soriano, A. Raso, J. Mcksch, M. Feingold, G. Rivas, and P. Schwill, Treadmilling analysis reveals new insights into dynamic ftsz ring architecture, *PLOS Biology* **16**, e2004845 (2018).
- [53] G. Rivas, A. Lpez, J. Mingorance, M. J. Ferrndiz, S. Zorrilla, A. P. Minton, M. Vicente, and J. M. Andreu, Magnesium-induced linear self-association of the ftsz bacterial cell division protein monomer: The primary steps for ftsz assembly, *Journal of Biological Chemistry* **275**, 11740 (2000).
- [54] B. Monterroso, M. . Robles-Ramos, M. Sobrinos-Sanguino, J. R. Luque-Ortega, C. Alfonso, W. Margolin, G. Rivas, and S. Zorrilla, Bacterial division ring stabilizing zapa versus destabilizing slma modulate ftsz switching between biomolecular condensates and polymers, *Open Biology* **13**, 220324 (2023).
- [55] A. K. Sharma, S. M. Poddar, J. Chakraborty, B. S. Nayak, S. Kalathil, N. Mitra, P. Gayathri, and R. Srinivasan, A mechanism of salt bridge-mediated resistance to FtsZ inhibitor PC190723 revealed by a cell-based screen., *Molecular biology of the cell* **34**, ar16 (2023).
- [56] D. Popp, M. Iwasa, A. Narita, H. P. Erickson, and Y. Maéda, FtsZ condensates: An in vitro electron microscopy study, *Biopolymers* **91**, 340 (2009).
- [57] A. Stukowski, Visualization and analysis of atomistic simulation data with OVITO-the Open Visualization

- Tool, Modelling and Simulation in Materials Science and Engineering **18**, 10.1088/0965-0393/18/1/015012 (2010).
- [58] R. E. Isele-Holder, J. Elgeti, and G. Gompper, Self-propelled worm-like filaments: spontaneous spiral formation, structure, and dynamics, *Soft Matter* **11**, 7181 (2015).
- [59] S. Plimpton, *J. Comput. Phys.* **117**, 119 (1995).
- [60] P. G. de Gennes, *Scaling Concepts in Polymer Physics* (Cornell University Press, New York, 1979).
- [61] J. A. Aronovitz and D. R. Nelson, Universal features of polymer shapes, *J. Phys. France* **47**, 1445 (1986).
- [62] J. W. Cannon, J. A. Aronovitz, and P. J. Goldbart, Equilibrium distribution of shapes for linear and star macromolecules, *J. Phys. I France* **1**, 629 (1991).
- [63] R. I. Dima and D. Thirumalai, Asymmetry in the shapes of folded and denatured states of proteins, *J. Phys. Chem. B* **108**, 6564 (2004), arXiv:0310023 [q-bio].
- [64] R. Hegger, H. Kantz, and T. Schreiber, Practical implementation of nonlinear time series methods: The tisean package, *Chaos* **9**, 413 (1998).
- [65] S. C. Takatori, W. Yan, and J. F. Brady, Swim pressure: Stress generation in active matter, *Phys. Rev. Lett.* **113**, 028103 (2014).
- [66] X. Yang, M. L. Manning, and M. C. Marchetti, Aggregation and segregation of confined active particles, *Soft Matter* **10**, 6477 (2014).
- [67] J. Bialké, J. T. Siebert, H. Löwen, and T. Speck, Negative interfacial tension in phase-separated active brownian particles, *Phys. Rev. Lett.* **115**, 098301 (2015).
- [68] A. P. Solon, J. Stenhammar, R. Wittkowski, M. Kardar, Y. Kafri, M. E. Cates, and J. Tailleur, Pressure and phase equilibria in interacting active brownian spheres, *Phys. Rev. Lett.* **114**, 198301 (2015).